Multi-Scalar Measurements in Hydrogenated Bluff-Body Stabilized Turbulent Flames Using 1D Spontaneous Raman Scattering and OH -PLIF

Kuppuraj Rajamanickam, A. M.Mahuthannan, Saïd Idlahcen, Bertrand Lecordier, Corine Lacour, Armelle Cessou, David Honoré

Multi-Scalar Measurements in Hydrogenated Bluff-Body Stabilized Turbulent Flames Using 1D Spontaneous Raman Scattering and OH -PLIF

K. Rajamanickam[1,2], A. Mahuthannan[3], S. Idlahcen[1], B. Lecordier[1], C. Lacour[1], A. Cessou[1], D. Honoré[1]*

[1]CORIA - CNRS, UNIROUEN, INSA Rouen, Normandie Univ; 675 Avenue de l'université, 76801 Saint-Etienne-du-Rouvray, France.
[2]Department of Mechanical Engineering, Imperial College London, Exhibition Rd, London, SW7 2AZ
[3]SINTEF Energy Research – NTNU, Høgskoleringen 1, 7034 Trondheim, Norway

Abstract

This paper examines the effect of H_2 enrichment in a primary fuel (CH_4) using 1D spontaneous Raman scattering (SRS) and OH-PLIF measurements. The experiments are conducted in a canonical non-premixed bluff body burner operating under typical central fuel jet-dominated flow mode. Downstream of the bluff body, the flow exhibits complex patterns, and it can be globally categorized into three successive zones: recirculation, neck, and jet-like zones. The flame undergoes local extinction in the neck zone, where the local flow-induced hydrodynamic strain rate (κ_{hyd}) is much higher than the flame extinction strain rate (κ_{ext}). It is well known that H_2 enrichment increases (κ_{ext}), and thus modifies the probability of localized flame extinctions in the neck zone. To understand this phenomenon, four H_2 enrichment levels are considered: 0%, 10%, 30%, and 50% (in vol.). The OH-PLIF measurements reveal the presence of local extinctions in the cases of H_2 enrichment $\leq$ 30%, while local extinctions are not witnessed for H_2 = 50%. 1D SRS measurements are implemented at different axial heights above the burner to identify the interlink between H_2 addition, local extinction, and scalar structure. The evolution of instantaneous and simultaneous distributions of multiple species (C.O., CO_2, N_2, O_2, CH_4, H_2, H_2O) concentrations and temperature are meticulously analyzed using various conditional statistics to gain insights into the non-premixed bluff-body stabilized hydrogenated turbulent flames.

1. Introduction

Hydrogen (H_2) is a promising energy source in decarbonizing combustion systems, as it can be readily produced on large scales from renewables. However, a significant difference in the thermophysical properties of H_2 in comparison with conventional fuels (e.g., CH_4) causes several operational challenges. For instance, the higher reactivity and higher flame temperature of H_2 lead to flashback and NOx emissions. Besides, the increased extinction strain rate (κ_{ext}) due to H_2 enrichment (Shanbhogue et al., 2016), (Zhang et al., 2022) is expected to alter the flame shape significantly. (Chterev and Boxx, 2021) highlighted the transition from an M-shaped flame to a shear-layer stabilized V-flame with H_2 enrichment in the swirl-stabilized flames. Furthermore, several studies (Barbosa et al., 2007) (Indlekofer et al., 2021) reported modifications in the combustion instabilities with H_2 addition.

Hence, more profound insights into the turbulence-chemistry interactions in H_2 flames are essential. For these reasons, canonical burner configurations are often employed, which provide access to investigation on various proportions of H_2 addition. In the present study, experiments are carried out in a canonical non-premixed bluff body burner with three different levels (10%, 30%, and 50% in vol.) of H_2 enrichment to the CH_4. Simultaneous measurements of the flow field and flame fronts are performed using time-resolved PIV & OH PLIF systems. Besides, 1D Spontaneous Raman Scattering (SRS) is implemented across various axial heights above the burner. The trends in the local extinction and subsequent evolution of local flame structure with the H_2 enrichment are explained based on the instantaneous temperature profile in mixture fraction space.

2. Canonical Burner Configuration and Operating Conditions

The schematic of the non-premixed canonical bluff body burner employed in this study is illustrated in **Figure 1**. It comprises of annular air passage and a central fuel injection port embedded with the cylindrical bluff body. The fuel flow rates of CH_4 and H_2 are varied in reference to the critical experimental parameter, namely, the volumetric concentration proportions of H_2 (α_{H2}). All the fluid flow rates are precisely controlled using thermal mass flow meters (*Bronkhorst*). Throughout all the test conditions, the thermal output of the burner (**Table 1**) and annular airflow rate have been maintained constant; the latter allowed us to keep the same aerodynamic features close to the burner exit.

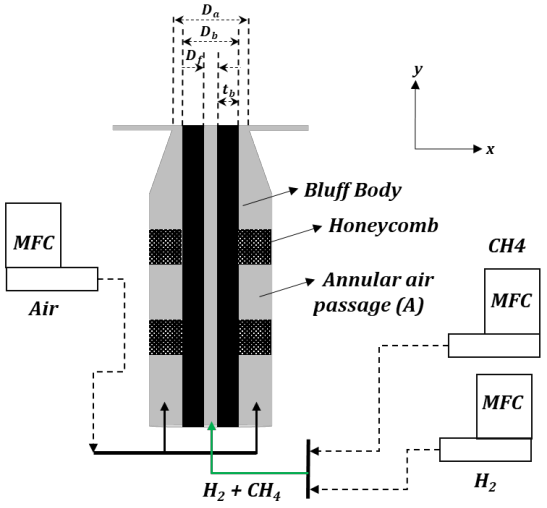

Figure 1. Configuration of a canonical non-premixed bluff-body burner.

*Corresponding author: david.honore@coria.fr

Table 1. Operating conditions

(α_{H2})	Re_{fuel}	Re_{air}	Power (kW)	$MR = \left(\frac{\rho_{air}U_{air}^2}{\rho_f U_f^2}\right)$
0	4370	10575	16.8	0.25
0.1	4300	10575	16.8	0.26
0.3	4123	10575	16.8	0.31
0.5	3872	10575	16.8	0.38

3. Diagnostic Techniques

a. 1D Spontaneous Raman Scattering (SRS)

A simplified schematic of the 1D SRS diagnostics tool employed in this study is shown in **Figure *2***. A detailed schematic can be found in (Ajrouche et al., 2015).

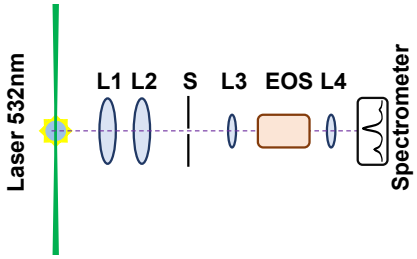

Figure 2. Schematic of Spontaneous Raman Scattering (L1 = 150 mm; L2 = 300 mm; L3 =200 mm; L4=300 mm)

A high-power (~1.8 mJ/pulse at 532 nm) laser (second harmonic of Nd: YAG) pulsing at 10 Hz is used. A spherical lens (*f=1000mm*) focuses the laser beam into the desired probe volume. Raman signal in the orthogonal direction is collected and refocused on a slit (S) using two achromatic lenses (L1 & L2). The slit allows lights only from the region of interest (ROI). Lens (L3) is used to collimate the light, and L4 is used to focus the light on the entrance slit of the spectrometer. Electro-Optic Shutter (EOS) consists of two polarizers and a Pockels cell between L3 and L4. The readout time of the eMCCD (PIXIS 400) camera used with the spectrometer (Princeton Instruments, IsoPlane SCT 320) is much larger than the laser pulse width (1000 ns). Thus, EOS minimizes the flame luminosity during such long exposure. The eMCCD has a resolution of 1340*400 pixels. The vertical 400 pixels are binned (hardware level before readout) into 8 ROIs covering 3.44 mm of probe length. The edge ROIs are removed during the post-processing due to the poor signal, which brings down the effective probe length to 2.58 mm in 6 simultaneous neighbored measurement locations with 430 µm spatial resolution each.

Furthermore, the horizontal 1340 pixels covered the spectrum range from 567nm to 694nm. One thousand shots are recorded for each measurement location. The final post-processing convergence is slightly lower due to poor signal in some instantaneous shots. Measurements are carried out above the burner at six axial heights (y = 5mm; 10 mm; 20 mm; 35 mm; 45 mm; 60 mm). For each axial height, radial profiles are acquired at x = – 6mm to 30 mm with the steps of 2 mm. A robotic traverse system is employed to control the measurement positions precisely.

b. Flow field and OH – PLIF measurements

The velocity field and OH fluorescence have been measured simultaneously using time-resolved PIV & OH -PLIF systems at 5 kHz. More details on the system and post-processing can be found in (Rajamanickam et al., 2022).

4. Global Flow Field and Flame Structures

Figure 3 compares the mean flow fields of the test cases investigated in this study. Due to the axisymmetric nature of mean quantities, only the positive side of the radial coordinate is shown in **Figure 3**. Interestingly, despite a significant rise in the central fuel jet velocity (U_f) from 12 m/s to 20 m/s between $\alpha_{H2} = 0$ to $\alpha_{H2} = 0.5$, the global topology of mean flow field is (relatively) similar across all the test cases. This is because the low-density property of hydrogen and constant annular airflow rate keeps the momentum ratio (*M.R.*) approximately the same (**Table 1**). Thus, the flow topology remains relatively unaltered even with a high-velocity jump in a central fuel jet due to H_2 enrichment.

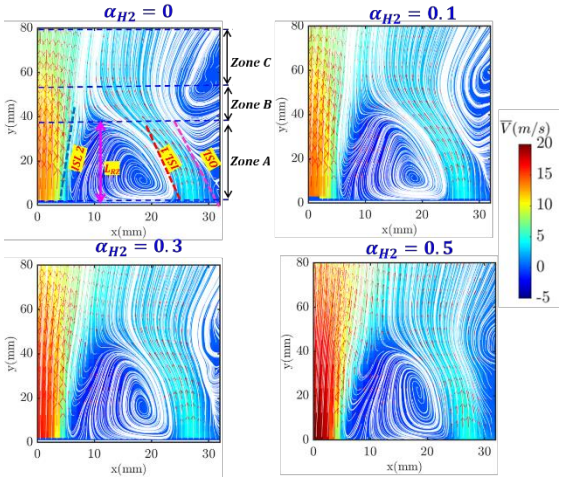

Figure 3. Time-averaged flow field across different H_2 enrichment levels.

Three distinct flow zones are identified based on the height above the burner (**Figure 3;** $\alpha_{H2} = 0$). The first zone (Zone A) comprises a strong air Recirculation Zone (R.Z.) induced immediately downstream of the bluff body exit. Here, the length of R.Z. $(\boldsymbol{L_{RZ}})$ is marked based on the average location of the stagnation point at the end of R.Z. Furthermore, three shear layers are witnessed in Zone A (see **Figure 3;**$\alpha_{H2} = 0$), (i) Outer shear layer (OSL) formed between the outer boundary of annular air jet and ambient air; (ii) Inner shear layer 1 (ISL1) separates the inner and outer boundaries of the annular air jet and R.Z., respectively. (iii) Inner shear layer 2 (ISL2) is induced between the inner boundary of R.Z. and the central fuel jet. Next to R.Z., the annular airflow converges towards the central fuel jet in the small region of $40\ mm \leq y \leq 55\ mm$.

This is referred as neck zone (Zone B). Finally, zone C resembles a jet-like flow structure downstream of Zone B. The obtained flow structure is classically referred to as "*central jet-dominated flow*" in the non-premixed bluff body flame literature (Roquemore et al., 1986). This corresponds to typical aerodynamic conditions ensuring turbulent flame stabilization thanks to the R.Z. obtained in our study for all hydrogen proportions.

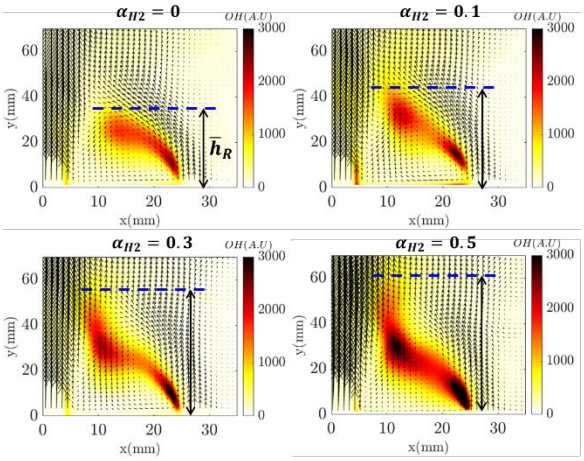

Figure 4. Mean flame structures of different H_2 enrichment cases obtained from OH -PLIF

Despite similar global flow topologies (**Figure 4**) across all the values of α_{H2}, there exists strong variations in the mean reaction zone height ($\bar{h}_R$) obtained from OH PLIF (**Figure 4**). For instance, the mean reaction zones of $\alpha_{H2} = 0, 0.1$ are found to be shorter and located within R.Z. On the other hand, for $\alpha_{H2} = 0.3, 0.5$, reaction zone is extended beyond the RZ. Interestingly, for all the cases, within RZ (i.e., Zone A), the flame is located in the shear layer formed between the outer and inner boundaries of RZ and the annular air jet, respectively (i.e., ISL1). This can be explained as follows, (i) First, part of the fuel from the central jet mixes with the air inside the RZ; (ii) The formed mixture is then convected radially outwards by strong air-driven RZ; (iii) Finally, the reaction is established in the ISL1, probably due to the local establishment of stoichiometry (or $\phi = 1$) in that region. This is consistent with the observation made by (Dally et al., 1998) in a similar bluff body burner configuration. Furthermore, in line with the above-made discussions concerning different flow regimes, the flame switches its path from ISL1 to ISL2 in the neck zone (i.e., zone B) and then resembles a jet-like flame configuration in zone C.

Figure 5a compares the radial profiles of mean and RMS temperature and mixture fraction obtained at different axial heights above the burner exit. Mixture fraction (ξ) is calculated based on Brigler's formulation (Bilger, 1989).

$$\xi = \frac{\frac{2(Y_c - Y_{c,Ox})}{W_c} + \frac{(Y_H - Y_{H,Ox})}{2W_H} - \frac{(Y_O - Y_{O,Ox})}{W_O}}{\frac{2(Y_{c,F} - Y_{c,Ox})}{W_c} + \frac{(Y_{H,F} - Y_{H,Ox})}{2W_H} - \frac{(Y_{O,F} - Y_{O,Ox})}{W_O}}$$

Where 'Y' represents elemental mass fractions of Carbon (C), Oxygen (O), and Hydrogen (H); '*W*' represents atomic weights. The subscripts F and Ox denote fuel and oxidizer, respectively. Inside the RZ, the mean mixture fraction is found to be overall lean in the radial region span of x = 10 -20 mm (**Figure 5**a). Across all the test cases, the largest gradients of mean mixture fraction (ξ_{mean}) occur at ISL2. Furthermore, the maxima of ξ_{rms} is also found to be aligned with the region where the ξ_{mean} exhibits a steep gradient. The ξ_{rms} shows nearly zero fluctuations in the central fuel jet within zone A. However, in zones B and C, it does fluctuate due to an increase in the U_{rms}, V_{rms} in that region (**Figure 5**b) because of strong air-fuel jet interactions. For all the H_2 enrichment levels, the mean temperature (T_{mean}) inside the RZ exhibits a broader high-temperature region of $7 < x < 25$ mm due to the recirculation of hot combustion products. On the other hand, T_{mean} become progressively narrower in zone B and zone C (i.e., $y \geq 35\ mm$) due to the jet-like flame structure. In line with the mean OH profiles shown in **Figure 4**, a decrease in the T_{mean} is noticed at y = 45 mm; 60 mm (i.e., downstream to the RZ) for $\alpha_{H2} = 0, 0.1$ (marked with arrows in **Figure 5**a). The physical interpretation behind this will be explained in more detail in the next section. As the fluctuations of ξ_{rms} increased in the zone B and C (**Figure 5**a; y =35mm; 45 mm; 50mm) due to an increased U_{rms} and V_{rms} which eventually causes high fluctuations in the temperature (T_{rms}).

5. Instantaneous Flame Structures and Scalar Profiles

This section presents instantaneous OH profiles and scatter plots of scalars in mixture fraction space to gain further insights into the spatial evolution of temperature relative to the H_2 enrichment. Attention is focused on the neck zone, where a drastic difference in $T_{mean}$is observed between $\alpha_{H2} = 0, 0.1$and $\alpha_{H2} = 0.3, 0.5$. Previous studies (Dally et al., 1998) (Masri et al., 1988) highlighted the occurrence of local extinctions in the neck zone as the flame undergoes excessive stretch due to the larger radial velocity gradients associated with the annular airflow in that region (convective centripetal influx). **Figure 6** illustrates the instantaneous OH profiles of different H_2 enrichment cases in the neck zone. The overlaid black contours represent the flame topology from OH PLIF images, and the color contours denote the 2D hydrodynamic strain rate (κ_{hyd}- norm of the strain rate obtained from the PIV velocity field) acquired at the same time instant. The flame undergoes local extinction as a consequence of interaction with a high strain of 5000 s^{-1} in the ISL2 (**Figure 6**; $\alpha_{H2} = 0$ -t = 0.4 ms; $\alpha_{H2} =$ 0.3- t = 0.2 ms). On the contrary, as illustrated in (**Figure 6** $\alpha_{H2} = 0.5$), local extinctions are no longer witnessed despite the strong interaction of flame fronts with the high strain rate in the ISL 2. The increased H_2 content intensifies the extinction strain resistance of flame (κ_{ext}) (Shanbhogue et al., 2009) over the fluid

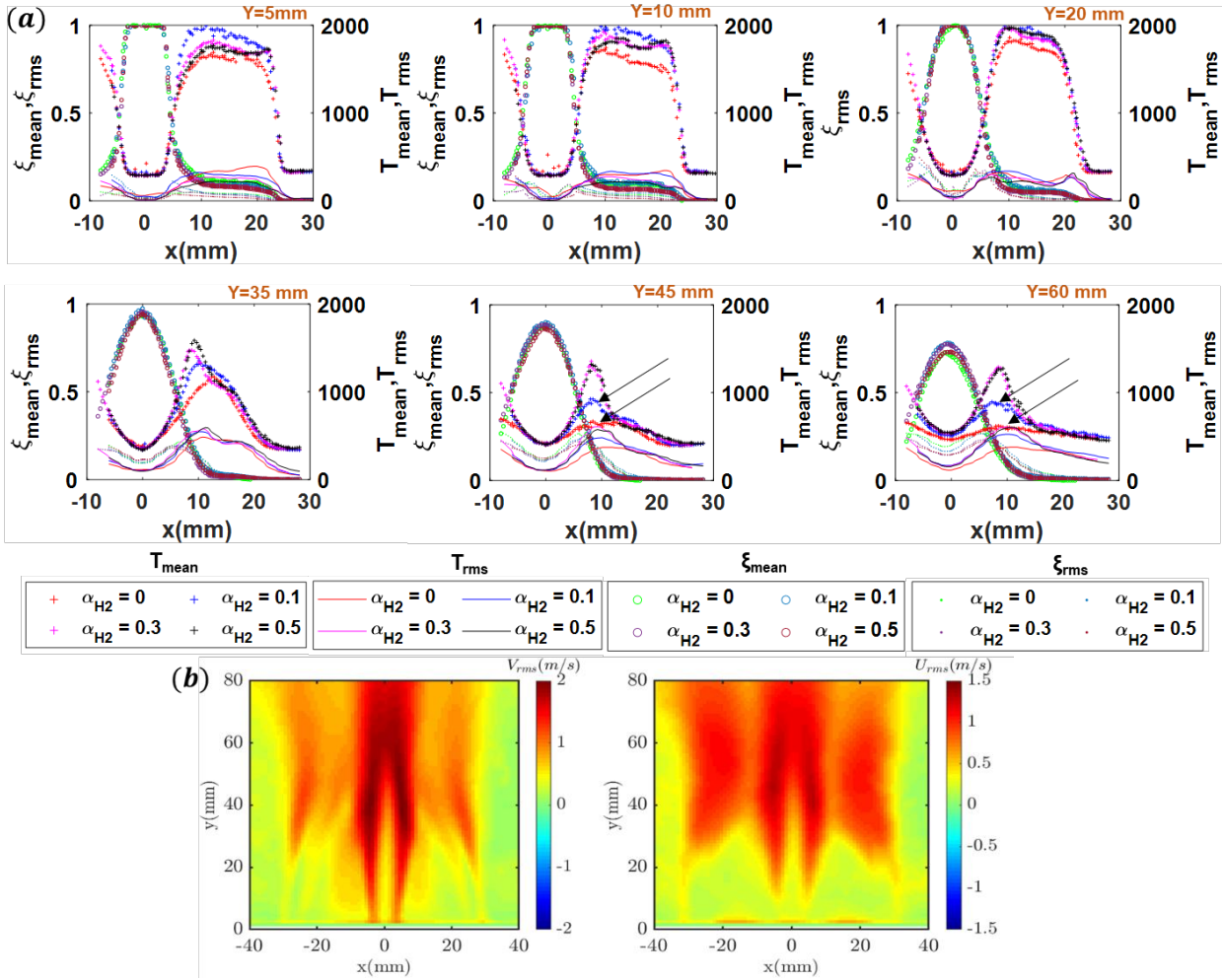

Figure 5. a. Radial profiles of the mean (+) and RMS (solid lines) temperature, mean (o), and RMS (dots) mixture fraction [Top row – Zone A; Bottom row – Zone B, C]; b. RMS contours of axial and radial velocity ($\alpha_{H2} = 0.1$).

dynamic strain (κ_{hyd}) and thereby prevents local extinction. Furthermore, following the flame branches are witnessed for the test case $\alpha_{H2} = 0.3$ (**Figure 6**). On the other hand, failure of the reconnection of flame branches is noticed for non-hydrogenated flame (**Figure 6**; $\alpha_{H2} = 0$). Two reignition mechanisms, edge flame propagation and turbulence mixing by adjacent vortices, are widely reported in non-premixed turbulent jet flames. (Briones et al., 2008) and (Frouzakis et al., 2002) have shown that H_2 enrichment to the methane leads to a progressive rise in the edge flame speed due to enhanced reactivity and preferential diffusion. Thus, an increase in the edge flame speed with H_2 enrichment leads to quicker reconnection of the broken branches that formed due to the local extinction. **Figure 7**a illustrates the scatter plots of instantaneous temperature and oxygen mass fractions (Y_{O2}) colored relatively to the burner's radial positions. The vertical solid (blue) line on the temperature scatter plot represents the stoichiometric mixture fraction (ξ_{st}). Here, x = 6 – 12 mm (colored with green) is the radial region where the local extinctions are majorly observed (see **Figure 7**). As discussed earlier, for the test cases of $\alpha_{H2} = 0, 0.1$, failure of reconnection of the broken flame branches following the local extinction resulted in the distribution of samples in the low-temperature region (green-colored dots in **Figure 7**a; $\alpha_{H2} = 0, 0.1$). The increase in Y_{O2} in the same region **Figure 7**b; $\alpha_{H2} = 0, 0.1$) further supports this observation. On the other hand, quicker reconnection of the flame branches following the local extinction and the absence of local extinction leads to higher temperatures in the region x = 6 – 12 mm for $\alpha_{H2} = 0.3$ and $\alpha_{H2} = 0.5$, respectively (**Figure 7**a). It is interesting to note that, even for $\alpha_{H2} = 0.3,0.5$, small fraction of samples (marked with dotted circles in **Figure 7**a; $\alpha_{H2} = 0.3,0.5$) exhibits low temperature in the region of x = 6 – 24 mm. This is attributed to the radial flapping of flame caused by increased U_{rms} (**Figure 5**b) in that region.

Furthermore, conditional statistics are implemented to quantify the degree of local extinctions. This is done by conditioning the temperature data in the small mixture fraction window of $0.05 < \xi < 0.06$ (these values lie close to the stoichiometric mixture fraction). **Figure 7**c

compares the conditional pdfs of temperature distribution across different axial heights above the burner. Within zone A, i.e., RZ (**Figure 7**c; y= 5mm, 20 mm), the obtained temperature exhibits unimodal distribution across all the test cases. This is due to the absence of local extinctions inside the RZ. However, a bimodal distribution is witnessed in the axial heights of Y ≥ 35mm (i.e., zones B and C), which is attributed to the two phenomena: local extinctions and flame flapping. The probability of high-temperature samples is progressively reduced, and it possesses broadened distribution of T = 1250 – 2250 K for $\alpha_{H2} = 0{,}0.1$ (**Figure 7**c; y > 35 mm). For the same cases, it should also be noted that there is a drastic increase in distribution in the low-temperature region of T = 400-600 K. In particular, this is more pronounced for $\alpha_{H2} = 0$ due to the high degree of local extinctions and failure of reconnection of flame branches after the local extinction, as illustrated in **Figure 7** ($\alpha_{H2} = 0$). For the cases of $\alpha_{H2} = 0.3, 0.5$, although there is reduction in the probability of samples (**Figure 7**c) in the high-temperature region, unlike, $\alpha_{H2} = 0{,}0{,}1$, distribution still peaks at T ~ 2100 K. As illustrated in **Figure 7** ($\alpha_{H2} = 0.3{,}0.5$), the absence of local extinctions/ quicker reconnection of broken flames due to increase in the edge flame speed leads to high temperature in the downstream regions, i.e., y = 45 mm, 60 mm.

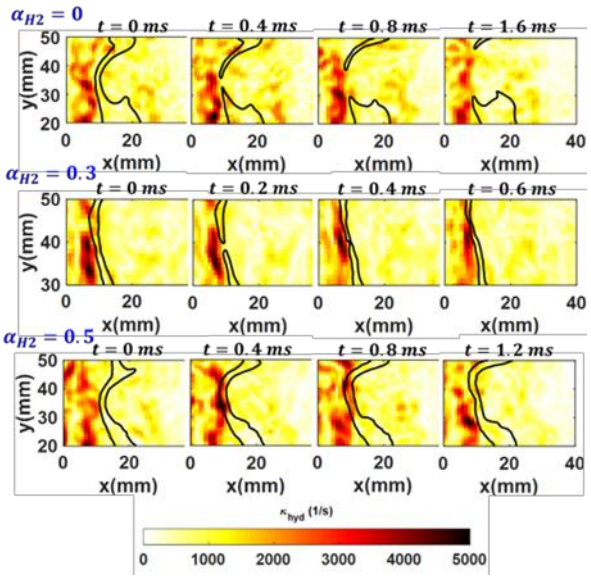

Figure 6. Time sequences of superimposed PIV strain field (color contours) and OH-PLIF (black contours) images illustrating the flame's interaction with high strain in the neck zone.

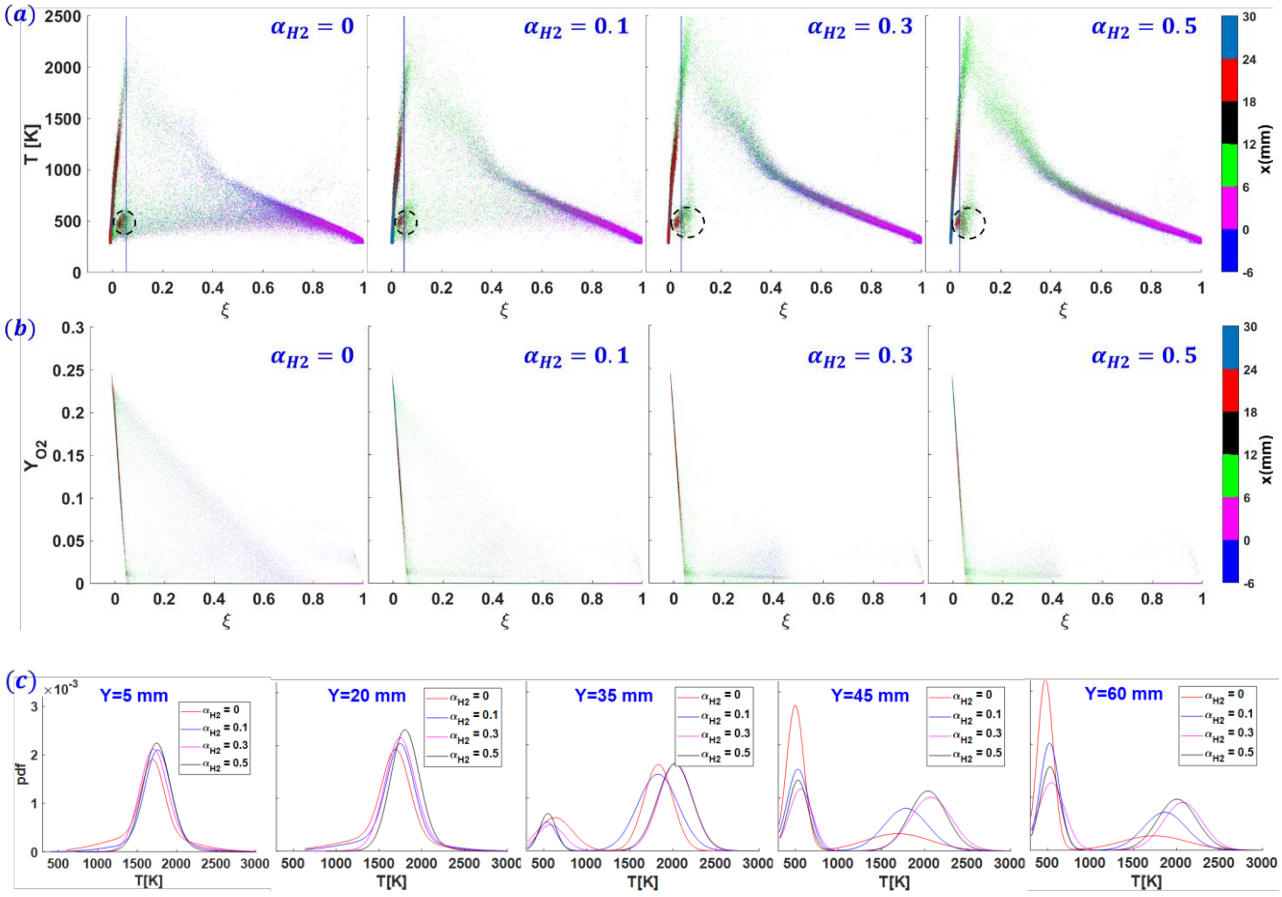

Figure 7. a. and b. Scatter plots of temperature and oxygen mass fraction (Y_{O2}) in mixture fraction space at y = 45 mm; c. Conditional pdfs of the temperature in the small fraction window ($0.05 < \xi < 0.06$) for different α_{H2} values.

6. Conclusions

This work discusses the impact of H_2 enrichment to the primary fuel CH_4 on the local flame structures in a canonical non-premixed bluff body burner. 1D SRS and simultaneous time-resolved PIV and OH-PLIF are employed to provide deeper insights into the turbulence-chemistry interactions. The evolution of radial profiles of temperature and scalars relative to different H_2 enrichment levels are presented across various axial heights above the burner. The scatter plots of temperature and oxygen mass fraction (Y_{O2}) in the mixture fraction space highlighted the presence of localized flame extinctions in the neck zone and subsequent reduction of temperature in the downstream region for the $\alpha_{H2} = 0{,}0.1$ flames. The results also revealed the absence of local extinctions for $\alpha_{H2} = 0.5$ due to the increased extinction strain rate over the local flow-induced hydrodynamic strain rate ($\kappa_{ext} > \kappa_{hyd}$).

7. Acknowledgments

This research work is supported by Normandie Regional Council and European Union through European Regional Development Fund (ERDF) in the framework of the RAPHYD project (RIN 2018). A. Mahuthannan's stay at the CORIA laboratory was part of a research collaboration with SINTEF and NTNU, funded by the OXYFUN project under the Research Council of Norway (grant number 268369).

8. References

Ajrouche, H., Lo, A., Vervisch, P., Cessou, A., 2015. Assessment of a fast electro-optical shutter for 1D spontaneous Raman scattering in flames. Measurement Science and Technology 26, 075501.

Barbosa, S., Garcia, M. de L.C., Ducruix, S., Labegorre, B., Lacas, F., 2007. Control of combustion instabilities by local injection of hydrogen. Proceedings of the combustion Institute 31, 3207–3214.

Bilger, R.W., 1989. The structure of turbulent nonpremixed flames, in: Symposium (International) on Combustion. Elsevier, pp. 475–488.

Briones, A.M., Aggarwal, S.K., Katta, V.R., 2008. Effects of H2 enrichment on the propagation characteristics of CH4–air triple flames. Combustion and Flame 153, 367–383.

Chterev, I., Boxx, I., 2021. Effect of hydrogen enrichment on the dynamics of a lean technically premixed elevated pressure flame. Combustion and Flame 225, 149–159.

Dally, B.B., Masri, A.R., Barlow, R.S., Fiechtner, G.J., 1998. Instantaneous and mean compositional structure of bluff-body stabilized nonpremixed flames. Combustion and Flame 114, 119–148.

Frouzakis, C.E., Tomboulides, A.G., Lee, J., Boulouchos, K., 2002. From diffusion to premixed flames in an H2/air opposed-jet burner: the role of edge flames. Combustion and Flame 130, 171–184.

Indlekofer, T., Ahn, B., Kwah, Y.H., Wiseman, S., Mazur, M., Dawson, J.R., Worth, N.A., 2021. The effect of hydrogen addition on the amplitude and harmonic response of azimuthal instabilities in a pressurized annular combustor. Combustion and Flame 228, 375–387.

Masri, A.R., Bilger, R.W., Dibble, R.W., 1988. Turbulent nonpremixed flames of methane near extinction: mean structure from Raman measurements. Combustion and Flame 71, 245–266.

Rajamanickam, K., Lefebvre, F., Gobin, C., Godard, G., Lacour, C., Lecordier, B., Cessou, A., Honore, D., 2022. On the relationship between H2 addition, local extinction and hydrodynamic instability in non-premixed bluff-body stabilized flames, in: 20th International Symposium on the Application of Laser and Imaging Techniques to Fluid Mechanics, Lisbon, Portugal.

Roquemore, W.M., Tankin, R.S., Chiu, H.H., Lottes, S.A., 1986. A study of a bluff-body combustor using laser sheet lighting. Experiments in Fluids 4, 205–213.

Shanbhogue, S.J., Husain, S., Lieuwen, T., 2009. Lean blowoff of bluff body stabilized flames: Scaling and dynamics. Progress in Energy and Combustion Science 35, 98–120.

Shanbhogue, S.J., Sanusi, Y.S., Taamallah, S., Habib, M.A., Mokheimer, E.M.A., Ghoniem, A.F., 2016. Flame macrostructures, combustion instability and extinction strain scaling in swirl-stabilized premixed CH4/H2 combustion. Combustion and Flame 163, 494–507.

Zhang, F., Zirwes, T., Wang, Y., Chen, Z., Bockhorn, H., Trimis, D., Stapf, D., 2022. Dynamics of premixed hydrogen/air flames in unsteady flow. Physics of Fluids 34, 085121.